International Journal of Coal Geology 159 (2016) 183–193

Contents lists available at ScienceDirect

International Journal of Coal Geology

journal homepage: www.elsevier.com/locate/ijcoalgeo

A microfluidic framework for studying relative permeability in coal

Alireza Gerami [a], Peyman Mostaghimi [a,*], Ryan T. Armstrong [a], Ali Zamani [a], Majid Ebrahimi Warkiani [b]

[a] School of Petroleum Engineering, The University of New South Wales, Sydney, Australia
[b] School of Mechanical and Manufacturing Engineering, Australian Centre for Nanomedicine, The University of New South Wales, Sydney, Australia

ARTICLE INFO

Article history:
Received 12 January 2016
Received in revised form 5 April 2016
Accepted 6 April 2016
Available online 13 April 2016

Keywords:
Relative permeability
Coal seam gas
Microfluidics
Micro-CT imaging

ABSTRACT

A significant unconventional energy resource is methane gas stored in shallow coal beds, known as coal seam gas. The flow and transport of fluid in coal beds occur in a well-developed system of natural fractures, called cleats. In this study, we developed an efficient workflow for the fabrication of microfluidic chips based on X-ray micro-Computed Tomography (micro-CT) images of coal. A dry and wet micro-CT imaging technique is utilized to image coal cleats that would be otherwise non-resolvable. The obtained image of the cleat network is then etched into silicon wafers and used to fabricate poly dimethyl siloxane (PDMS) microfluidic devices. Fluid transport and displacement efficiency are visualized and quantified in real time by injecting water with a flow rate of 1 μl min^{-1} into the fabricated cleat structure initially saturated with air. A microfluidic approach is used to measure the relative permeability of a realistic coal cleat system by monitoring the liquid recovery at recorded saturations after the breakthrough. Relative permeability curves show the cross and end point values for the water and gas flow, and predict a maximum relative permeability of 0.15 for the water phase. Understanding the relationship between coal cleat structure and the resulting relative permeability is crucial for the optimization of methane gas extraction and to reduce the environmental concerns of excess surface water production. Also, pore network modelling based on the Maximal Ball (MB) concept is applied to predict relative permeability curves numerically. Our experimental results are in good agreement with pore network modelling outcomes and provide consistent and smooth macro-scale relationships along with direct observation of the pore-scale physics. Therefore not only can the microfluidic approach be used as a validation tool for multiphase flow numerical models but it can also provide direct visualization of transport properties unique to coals. Overall, our developed system provides a better understanding of fluid flow behaviour in coal and presents novel relative permeability data for coal seam gas reservoirs under identical conditions and cleat sizes.

1. Introduction

Coal has been a viable source of energy for many centuries. Gas production from coal however is a recent and welcoming change (Hamawand et al., 2013). Decline in conventional resources, along with the environmental benefits of utilizing natural gas rather than coal has inclined the global interest to this alternative source of energy (Dabbous et al., 1974; Williams et al., 2012). Commercial extraction of methane from coal seam gas (CSG) reservoirs began in the United States in the 1970s. Exploration of CSG in Australia started in 1976, and the first commercial production occurred in 1996 in Queensland (Geoscience Australia, 2009). Since then, the CSG industry in Australia has developed rapidly, production was 2.8 billion m^3 for 2007 and 2008, and has risen to 6.2 billion m^3 in 2013 (Hamawand et al., 2013). Currently, CSG is an important and well-considered unconventional resource of energy in the United States, Australia, Canada, China, India and United Kingdom, with an estimation of around 256 Tm^3 of resources in these top-producing countries (Geoscience Australia, 2009; de Haas et al., 2013; Hamawand et al., 2013; Squarek and Dawson, 2006; Xu et al., 2014).

Methane gas is mostly stored in the coal matrix by adsorption, or as free gas in the larger pores or micro-fractures. As reservoir pore pressure reduces, the methane desorbs from the coal matrix surface and propagates towards the naturally developed micro-fractures, called 'cleats'. The cleats are originally saturated with water and thus as the gas is released a multiphase displacement process occurs (Harpalani and Schraufnagel, 1990). The rate of recovery from a coal seam reservoir is highly dependent on the porosity of the network, water saturation, and relative permeability of the system (Purl et al., 1991). Besides, a major environmental concern for CSG developments is surface water production, which is largely controlled by water phase relative permeability. The relative permeability of water in coal however is far from understood and available literature data varies significantly. Literature values for water phase coal relative permeability are displayed in

* Corresponding author at: School of Petroleum Engineering, Tyree Energy Technologies Building, The University of New South Wales, Sydney, NSW 2052, Australia.
E-mail addresses: peyman@unsw.edu.au (P. Mostaghimi), ryan.armstrong@unsw.edu.au (R.T. Armstrong), m.warkiani@unsw.edu.au (M.E. Warkiani).

http://dx.doi.org/10.1016/j.coal.2016.04.002
0166-5162/

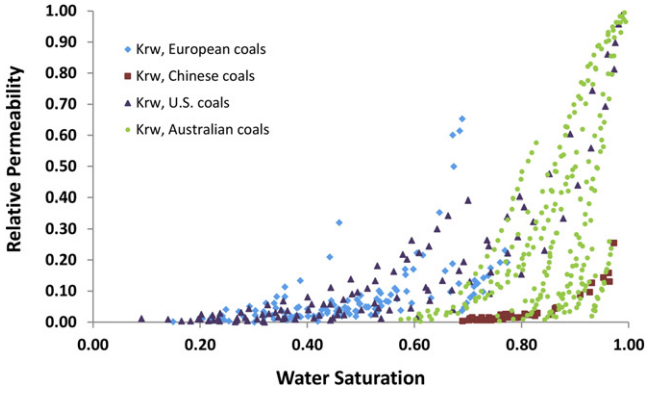

Fig. 1. Experimental data showing the water relative permeability for coals of various countries obtained from laboratory measurements and field production (Chen et al., 2014).

Fig. 1, which illustrates the wide range of relative permeability relationships that are possible. Typical techniques for collecting such data include laboratory core-flooding experiments and/or history matching to production data (Pan and Connell, 2012). Likewise a limited number of numerical and experimental studies have been reported for measuring and analysing absolute and relative permeability in coal (Ataie-Ashtiani et al., 2002; Blunt, 2000; Chen et al., 2013; Gash, 1991; Harpalani and Chen, 1995; Nguyen et al., 2013; Pan et al., 2010; Pant et al., 2012; Purl et al., 1991; Robertson and Christiansen, 2006; Wang et al., 2009; Zou et al., 2015).

Accurate measurement of relative permeability is of utmost importance for prediction of production rates (Blunt et al., 2013). It is well known that the relative permeability of a reservoir rock is highly dependent on the rocks underlying pore-scale structure, i.e. topology and geometry of the pore space. In a recent review (Zhang et al., 2014) it was highlighted that the relative permeability function for coal is far from understood. New methodologies for the measurement and evaluation of relative permeability results are required due to the unique structure of coal with cleat apertures ranging from 3 to 40 μm, small porosities in the range of 0.1% to 16%, and very low permeability of 0.1 to 100 md (Harpalani and Chen, 1997; Lamei Ramandi et al., 2015; Laubach et al., 1998; Meaney and Paterson, 1996; Radlinski et al., 2004). Additionally, there are the inherent difficulties in dealing with a brittle and deformable reservoir rock. In general, the relative permeability (K_{ri}) of phase i is defined as $K_{ri} = K_i / K$, where K_i is the effective permeability of phase i, and K is the absolute permeability. The corresponding effective permeability of phase i for a given saturation is calculated using the 2-phase extension of Darcy's Law (Dake, 1983)

$$K_i = \frac{q_i \mu_i L}{A \Delta P} \tag{1}$$

where μ is the viscosity of phase i, L is system length, A is cross sectional area normal to flow direction, Δp is the pressure difference, and q_i indicates the flow rate of phase i. This is a purely phenomenological approach in which the underlying physics are lumped into a saturation dependent relative permeability function, which provides no means to relate the underlying pore structure to the effective permeability. To select reservoirs with low water and high gas production rates, it is critical to understand the structural parameters in the coal cleat system that provide the wide range of relative permeability realizations (Fig. 1).

With conventional laboratory measurements however we are not able to quantitatively study the movement of fluids through the coal cleat system and correlate bulk measurements of relative permeability to the pore-scale topology and geometry of the cleat system.

Microfluidic studies are emerging in many biomedical and energy applications and can help to significantly reduce the cost of experiments while facilitating better process control and faster analysis in a dynamic fashion. In recent years, various types of microfluidic systems have been developed to study fluid flow behaviour inside a porous media for energy applications and/or oil recovery (Avraam and Payatakes, 1999; Joseph et al., 2013; Karadimitriou et al., 2012; Xu et al., 2014). For instance, Joseph et al. (2013) measured permeability in a microfluidic porous medium and studied the relationship between permeability and effective porosity. They designed a network, based on information obtained from sandstone rocks, and employed a computational network generation method called Delaunay triangulation. Xu et al. (2014) measured permeability in a periodic and random designed network. They found that the measured permeability in homogeneous pore networks is in reasonable agreement with the values estimated from the Carman-Kozeny equation. In another study, Avraam and Payatakes (1999) studied relative permeability for steady state flow in a network designed with a matrix of squares. None of these studies however attempted to make microfluidic chips with actual pore structures similar to features of real reservoir rock. More recent studies are devoted towards fabrication of microfluidic chips using geo-materials. For example, a new approach for fabrication of micro-channels inside geomaterials using laser etching and reactive ion etching (RIE) was developed and the rank and lithotype effect on coal wettability was explored (Mahoney et al., 2015a, 2015b). Porter et al. (2015) reported a direct visualization of flow behaviour inside natural fracture patterns. In another study, oil recovery in water flooding processes in periodic and random networks are compared, and the effect of pore size distribution and matrix geometry on displacement efficiency was explored (Xu et al., 2014). Gunda et al. (2011) fabricated a microfluidic chip with a network of reconstructed reservoir porous medium derived from scanning electron microscopy (SEM) images of actual samples. Delaunay triangulation was used, and the usual log distribution of pore sizes was adopted to extract a simplified network of pores and throats. They measured oil recovery in the micro-scale setup, which mimics the standard water flooding process. Thermal oil recovery has also been studied using microfluidic experiments (de Haas et al., 2013), and the effect of alkaline additive in oil recovery in two different grain size matrices was measured. Researchers also studied Bitumen oil production using CO_2 injection. They suggested microfluidic experiments to be easier, cheaper and safer to operate in comparison to conventional approaches (Fadaei et al., 2011; Lele et al., 2014). Song et al. (2014) used a real rock sample to fabricate a calcite microfluidic chip. They simulated an acid injection process, which is a secondary and tertiary oil recovery method, and visualized interactions between the matrix and acidified fluid.

Visualizing fluid flow in a 3D cleat system in real time is difficult, mainly due to the fast displacement and the complexity of the pore structure. A 2D microfluidic chip based on the cleat system representing the actual size and geometry of a real cleat structure, can easily display the multiphase flow behaviour and interactions within those complex structures. As can be seen in literature, 2D microfluidic studies in porous medium are being used and developed for several applications. However, multiphase flow in coal seams and its relative permeability have never been considered in these studies. Here we develop a novel workflow based on micro-computed tomography (micro-CT) imaging, Scanning Electron Microscopy (SEM) technology, and advanced image segmentation algorithms, to model exact coal cleat networks for the fabrication of a microfluidic device. We visualize flow in the coal cleat pattern, analyse contact angle and wettability effects, and simulate the gas recovery process. We measure relative permeability of a realistic coal structure network using microfluidic methodology, and validate our methodology by comparison of the results to literature values

and pore network simulations of the original 3D coal cleat network. The results can be used as benchmarks for validating numerical calculations and providing insights into fluid-fluid displacement in coal cleat systems.

2. Materials and methods

2.1. Coal sample imaging

X-ray micro-CT imaging is performed on a medium volatile bituminous coal, vitrinite reflectance of 1.15%, extracted from Moura mine, currently called Dowson mine, which lies in the Baralaba Coal Measure Formation, located 185 km southwest of Gladstone, Queensland, Australia (Lamei Ramandi et al., 2015). This formation was deposited during the late Permian times under fluvio-deltaic conditions (Dicks et al., 2004; Korsch et al., 1998). The coal geology of this field has been discussed in detail by Hawthorne (1975) and Mallett et al. (1995). A summary of the sample specifications is provided by Lamei Ramandi et al. (2015). A high-resolution, large-field, helical scanning instrument at Australian National University (ANU) is used to obtain images with the resolution of 16.5 μm. 3 mm aluminium X-ray beam filter is used to attenuate soft X-rays at the source. Also, a 28 mm × 35 mm radiographic field of vision, 23 hour acquisition time, and 120 kV X-ray energy are implemented to obtain the images. The micro-CT imaging details are described elsewhere (Golab et al., 2013). After imaging the dry coal sample (a full size core plug with 25 mm diameter and 35 mm length), it is saturated with 1.5 M Sodium Iodide (NaI) mixed with 1 M Potassium Chloride (KCl) brine to increase the X-ray attenuation of the coal fractures. The saturated (wet) core is imaged subsequently and registered to the dry image using the method developed by Latham et al. (2008). Subtracting the dry and wet images provides a difference image, which enables us to visualize features smaller than the scanner resolution.

After micro-CT imaging the sample is cut, parallel to butt cleats, and polished. SEM imaging is performed (Hitachi S3400, University of New South Wales, Australia) to obtain a high-resolution image of 100 nm resolution to visualize and measure apertures of the coal cleat system. Image segmentation is the process of converting a grey-scale multiphase image into two or more unique and well-defined phases (Mostaghimi et al., 2015). To segment the grey-scale image, we use data from SEM imaging and relate the micro-CT values to the measured aperture of the cleats in the SEM image. In Fig. 2 we provide a grey-scale and segmented image of our coal sample. Details of segmentation are described in Lamei Ramandi et al. (2015) and the references therein.

The grey-scale image is segmented into four phases: (1) resolved fractures includes fractures and pores that exist at or above the micro-CT resolution limit, (2) sub-resolution porous regions that exist below the micro-CT resolution limit, (3) mineral regions, and (4) solid matrix. After segmentation, the resolved cleat system is observed and a microfluidic chip is generated based on the measured features of the cleat geometry.

2.2. Microfluidic Chip fabrication

The cleat network dimensions are calibrated in ImageJ (1.48v, National Institutes of Health, USA) for 16.5 μm per pixel image resolution, and transferred to AutoCAD (Version 2014, Autodesk Inc.) software. Cleat network areas and solid regions are distinguished in the CAD file, and transferred into a chrome mask for microfabrication purpose. Silicon molds are fabricated using standard lithography techniques described previously (Warkiani et al., 2011). Single side polished 4 inch silicon wafers are patterned and etched using deep reactive ion etching (DRIE) to define the channel features on the wafer. The patterned silicon wafer is silanized with trichloro (1H, 1H, 2H, 2H-perfluorooctyl) silane to render the surface hydrophobic and facilitate release of the subsequent polydimethylsiloxane (PDMS) layer. PDMS prepolymer is prepared by mixing the PDMS at a standard 1:10 ratio and degassing in a desiccator. To produce the microfluidic chip, PDMS prepolymer is poured onto the silicon mold and cured at 80 °C for 1–2 h inside an oven. The PDMS is then cut from the mold, and fluidic access holes (one-inlet and one-outlet) are punched. Microscopic glass slides along with the PDMS chips are then rinsed thoroughly with isopropanol for 10 min and blown dry using N_2. The PDMS chips are bonded to the PDMS coated glass slides (Karadimitriou et al., 2013) to complete the channels by treating them for 2 min in an oxygen plasma machine (Harrick Plasma Cleaner, NY, USA). Following plasma treatment, the surfaces are immediately brought into contact with each other and allowed to cure for 3 h to complete the bonding before testing.

A thick layer of PDMS is used for the chip to reduce the possibility of air diffusion from the top cover. The final microchip has a stable wettability with the desired contact angle value similar to contact angles measured for coal (Saghafi et al., 2014). The porosity of the fracture system is calculated by dividing the porous volume to the total network volume, and a value of 10% porosity is measured, which is in the range of common coal seam samples (Lamei Ramandi et al., 2015). The general workflow for fabricating the microfluidic chip is shown in Fig. 3.

2.3. Experimental setup

High precision pressure pumps (AF1 Dual, Elveflow, Elvesys, Paris, France) and a high accuracy flow sensor (MFS1, Elveflow, Elvesys, Paris, France) are used to monitor and control the flow characteristics.

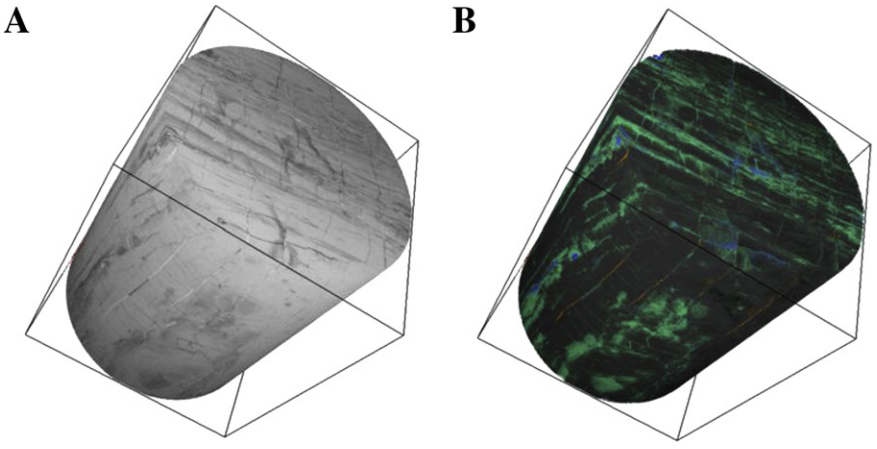

Fig. 2. (A) Grey-scale image obtained from micro-CT imaging, and (B) segmented image (blue = resolved pores and fractures, green = sub-resolution pores and fractures, black = macerals, orange = minerals).

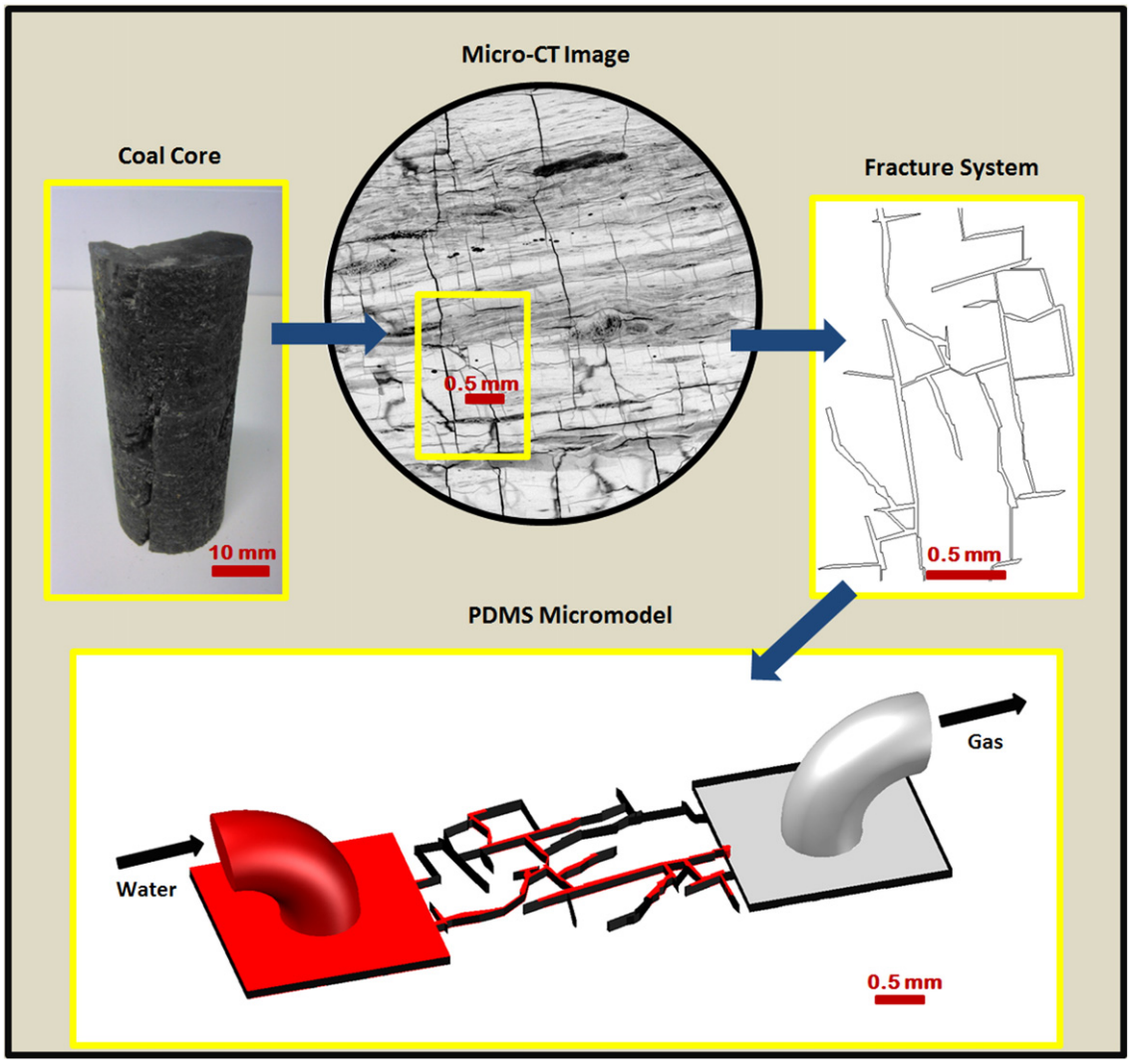

Fig. 3. Schematic workflow showing process of fabricating a microfluidic chip based on a real coal fracture structure obtained from micro-CT imaging.

Deionized water is mixed with 1.0 wt.% red food colour (AmeriColor, Placentia, CA, USA) for high contrast visualization, and passed through a 0.45 μm filter to eliminate residual particles. The sample is then pressurized in a reservoir (50 ml falcon tube with connection kit, Elvesys, Paris, France) and injected into the microfluidic chip at constant flow rates. Videos and images are taken using a CCD digital camera (OLYMPUS, DP80) coupled with an inverted microscope (OLYMPUS, IX73) with frame resolution of 1360 × 1024 pixels. Fig. 4 demonstrates the setup used for the presented experimental data.

The contact angle of Air/Water/PDMS is measured using optical contact angle meter (CAM 200, KSV Instruments Ltd, Helsinki, Finland) by imaging and measuring the angle of a dyed water drop on the PDMS surface. By performing image processing when the liquid is in motion, we find the dynamic contact angle for the system.

2.4. Relative permeability measurement

To measure the effective permeability, deionized water is injected into the fluidic channels at a constant flow rate of 1 μl min^{-1}. Using a feedback circuit between flow sensor and pump, the generated pressure is automatically adjusted to meet the desired injection flow rate. Variations of applied pressure are displayed and recorded on a computer as displayed in Fig. 4.

We capture images from the network saturation at multiple time sequences after the breakthrough of water at the outlet of the chip, and in each time step, water saturation (S_w) is measured using ImageJ and AutoCAD software. The effective permeability of water for the corresponding saturation is calculated using Eq. (1) where we use K_w for the effective permeability of water, $\mu = 0.9$ cp indicates the viscosity of dyed water, $\Delta L = 2.21$ mm is the length between inlet and outlet of the porous network, $A = 0.117$ mm^2 is the cross sectional area normal to flow direction, Δp is the pressure difference across the network, and q_w indicates the water flow rate at the outlet. We determine q_w by using the conservation of mass equation for an incompressible and unidirectional flow (Kirby, 2010) and by knowing the inlet flow rate, and the variation of water saturation over time. Pressure drop in the connecting tubes is calculated using Hagen-Poiseuille equation (Kirby, 2010) and subtracted from the measured pressure values to obtain the net capillary pressure values. Outlet is always connected to the atmosphere, and the experiment is conducted at ambient conditions. Dividing the effective permeability (K_w) to the absolute permeability (K) we calculate the relative permeability of the injecting water phase.

2.5. Network modelling

Network modelling is a well-established numerical method for prediction of absolute and relative permeability (Blunt, 2001; Blunt et al., 2002, 2013). The extracted network is used to simulate multiphase flow through a lattice of connected pores nodes and throats. The

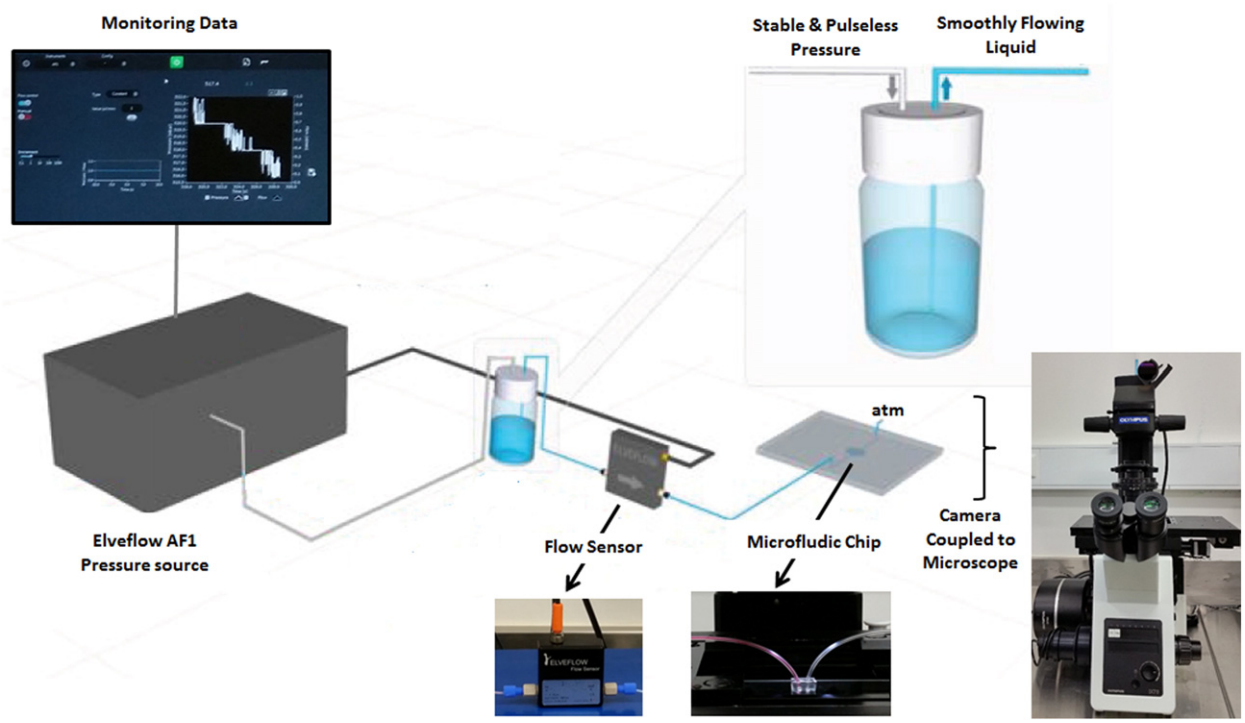

Fig. 4. Experiment setup for injection of fluid into the microfluidic chip. Water is pressurized in a reservoir and passed through flow sensor to obtain an injection rate of 1 μl min^{-1}.

network generation used here is based on the Maximal Ball (MB) concept that was introduced by Silin and Patzek (2006) and later modified by Dong and Blunt (2009). The MB finds the largest inscribed spheres touching the solid phase centred in each void voxel. After removing the inclusions, chains of remained MBs describe the pore space such that each ball is connected to the largest one as its ancestor. Having a common sphere in two or more MB chains leads to merging the smaller touching spheres inheriting the largest ones and thus creating connected pathways. The final outcome is a network of spheres connected by tubes representing pore nodes and throats, respectively. Fig. 5 shows the extracted network for a cubic subset of 1200 × 830 × 1120 voxels from the micro-CT image with a resolution of 16.5 μm. The MB defines 8432 balls connected by 24,582 throats giving average coordination number of 2.9.

Assuming mass conservation at each pore node (Oren et al., 1998), we obtain for fluid *i*

$$\sum_J q_{i,IJ} = 0 \tag{2}$$

where *J* indicates the pore nodes that are connected to pore node *I* and *q* is the flow to or from pore node *I*. Assuming the multiphase flow as

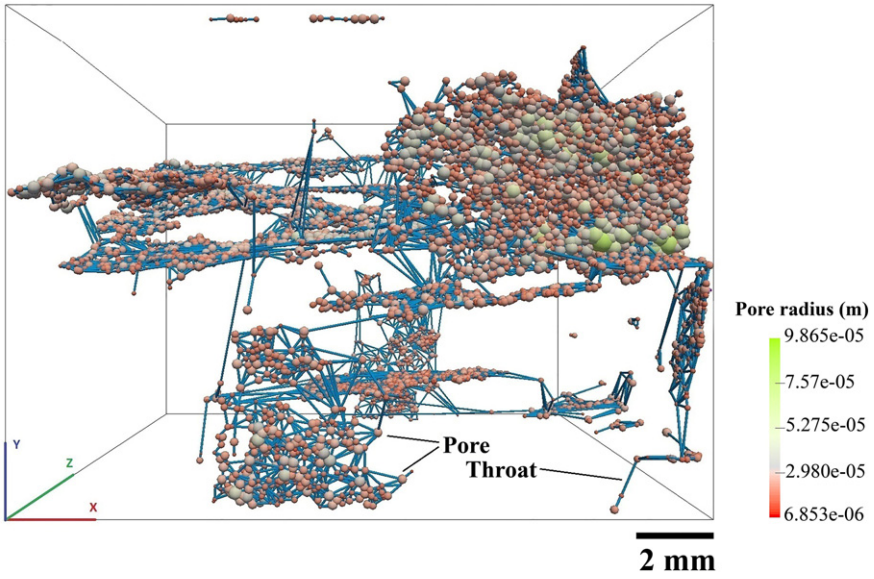

Fig. 5. Pore network model of the Moura coal sample with dimension of 1200 × 830 × 1120 voxels and resolution of 16.5 μm; spheres show the pore nodes and tubes show the connecting throats.

laminar, Newtonian, incompressible and immiscible makes the flow rate q related to pressure gradient ∇p as presented by Poiseuille law (Bakke and Øren, 1997)

$$q = -g\nabla p \tag{3}$$

where g represents the fluid conductivity and is a function of the elements cross sectional area, fluid viscosity and the dimensionless shape factor (Mason and Morrow, 1991). Conductance can be calculated via a variety of equations representing different pore node and throat shapes for different wettability conditions while fluids occupy either the centre or corners of the elements. The conductance of non-wetting phase that flows at the centre of pore nodes and throats is expressed by

$$g_i = \alpha \frac{A_i^2 G_i}{\mu} \tag{4}$$

where A_i is the cross section area of the ith element occupied by non-wetting phase, G_i is the dimensionless shape factor of the same element, μ is the viscosity of the fluid and α is a constant for different pore nodes or throats shape. The conductance for the wetting phase occupying the corners is calculated by

$$g_i = \frac{A_i^2}{C_i W_i \mu} \tag{5}$$

where C_i is the dimensionless flow resistance factor for reduced water conductivity close to the pore wall at strongly water-wet system with a contact angle of 0 (Oren et al., 1998) and W_i is given by

$$W_i = \frac{\cos\beta_i}{\sin\beta_i} - \frac{\pi}{2}\left(1 - \frac{\beta_i}{90}\right) \tag{6}$$

where β_i is the corner half angle. At the end, effective conductance for each phase is the harmonic mean of the conductance calculated for two pore nodes and the throat connecting them

$$\frac{L_{IJ}}{g_{i,IJ}} = \frac{L_t}{g_{i,t}} + \frac{1}{2}\left(\frac{L_I}{g_{i,I}} + \frac{L_J}{g_{i,J}}\right) \tag{7}$$

where the subscript t indicates the connecting throat while I and J point to the connected pore nodes, L_t, L_I and L_J represent the throat length and hydraulic radii of pore nodes, respectively and L_{IJ} is the distance of pore node centres. Pressure distribution at each node is computed by solving the linear system of equations corresponding to the network generated by Eq. (2). Applying arbitrary boundary pressures to solve the system of equations will result in multiphase permeability determination at a specific saturation. It should be mentioned that capillary pressure P_c is the factor that determines which element is invaded by the invading phase.

3. Results and discussion

3.1. Wettability

The wettability of the fabricated chip is found to be similar to contact angle values for methane/water/coal systems, previously measured by Saghafi et al. (2014) and indicated in Fig. 6. The result demonstrates a static contact angle of 73° (from the non-wetting fluid), and a dynamic contact angle of around 60°, which suggests an intermediate wettability for the system (Fig. 6). This is a unique characteristic of PDMS in its natural state and demonstrates the benefit of using PDMS for the coal representing chips since many other microfluidics studies required treatments of the PDMS to obtain wettability conditions similar to the reservoir rock of interest. Hence the experiment with untreated PDMS is considered to be a weakly gas-wet setup mimicking a natural coal seam gas reservoir. Also, the interfacial tension of methane and water is about 73 mN m^{-1} (Schmidt et al., 2007), which is similar to the interfacial tension of air and water that is around 72.8 mN m^{-1} (Vargaftik et al., 1983).

3.2. Cleat junction experiment

To calibrate and visualize the effect of wettability on the filling sequence, two sets of experiments at gas-wet and liquid-wet states are performed using a PDMS microfluidic chip with a simple cleat junction pattern. For the drainage experiment with a contact angle of 73°, DI water is injected into the chip that was initially filled with air at a constant flow rate of 1 μl min^{-1}. As can be observed in Fig. 7, drainage occurs in the order expected by the Young-Laplace capillary pressure equation (Lenormand et al., 1983), i.e. the largest channel of 200 μm becomes filled with non-wetting phase first. Lattice Boltzmann method (LBM) calculations, and experiments performed by Chapman et al. (2013) confirm these results. Knowing this filling sequence is important as it represents flow transport behaviour in coal seam gas reservoirs due to the similar wettability conditions. Hence, displacement in coal seams can be interpreted and pore network models can be developed with respect to this fluid flow behaviour.

For decane injection with the contact angle of 120°, which represents an imbibition process, the fluid travels along the narrowest adjacent channel first. Hence, the channel with the throat size of 50 μm is filled before other branches of the junction. In this liquid-wet experiment the contact angle is greater than 90°, which results in a negative

A

Methane/Water/Coal								
Pressure (Mpa)	1.8	5	7.7	9.6	11.7	13.2	13.7	15.3
Contact Angle (θ°)	88.9	81.9	78.4	86.9	85.6	76.3	78.8	81.1

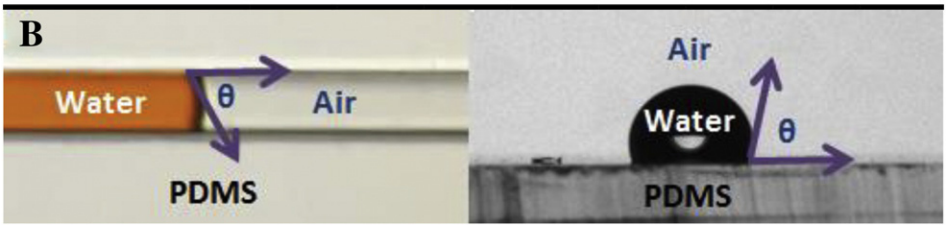

Fig. 6. A) Contact angles for Methane/Water/Coal system measured by Ref Saghafi et al. (2014) based on a captive gas bubble technique. B) Dynamic (left) and static (right) contact angle measurement for Air/Water/PDMS system. It represents the same contact angle for Methane/Water/Coal with the value of 73°. The system is intermediately gas-wet.

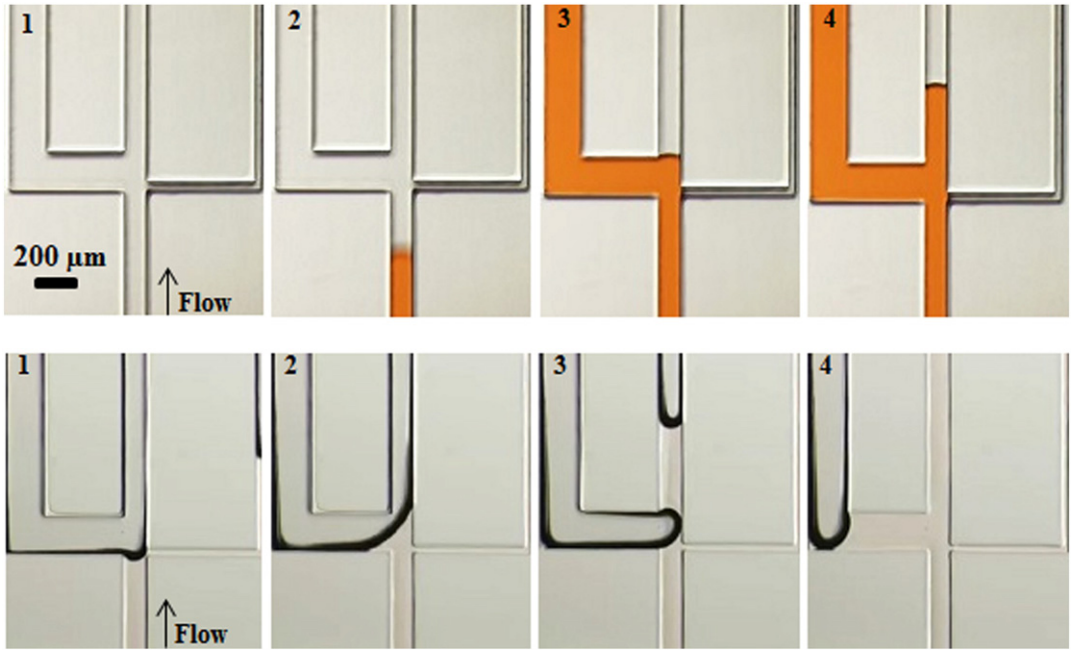

Fig. 7. Optical images showing filling sequences in a simple junction in both drainage (upper pictures), and imbibition (lower pictures) experiments.

capillary entry pressure as suggested by the Young-Laplace equation. This will cause the injected wetting phase to select the downstream branch with the highest capillary entry pressure first. Hence, the next adjacent narrowest channel which is a branch with 100 μm throat size will become filled. Here we can observe that the effect of wettability in the small pore sizes and micro-fractures of coal structure can play a role in recovery processes. By passing liquid through the micro-fracture, gas stored in smaller pores may remain unrecovered during the drainage process. Hence, increasing wettability and leading the system towards liquid-wet conditions could be suggested in enhanced recovery methods for CSG.

3.3. Gas recovery in cleat network

The filling sequence of water injection in the fabricated coal porous structure is presented in Fig. 8. Water (non-wetting fluid, coloured orange) is displacing gas (wetting fluid) at a rate of 1 μl min^{-1}. The pictures demonstrate that water follows the transport behaviour of a gas-wet system, and passes through the larger throats with the lowest capillary entry pressure. Traditional core flooding experiments cannot visualize a real time fluid flow and displacement in porous media. Trapped gas in both dead-end and open channels is observed in the images. Breakthrough occurs at 171 s, where the total fraction of gas displaced is 59.6%. The gas recovery curve over time (see Fig. 8) is measured via image processing of the captured filling steps using ImageJ and AutoCAD, and with the assumption of a 2-dimensional fluid system. During the flooding sequence, a total amount of 84% of the original trapped gas is recovered. The trend in gas saturation is in agreement with what was observed by Gunda et al. (2011) and Xu et al. (2014) in oil wet and gas wet experiments, and also with reported numerical prediction of gas recovery in coal seams (Zhang et al., 2015). The discrepancy in our results with their findings is perhaps due to different porous structures and boundary conditions, and also due to the small size of our system compared to them. There is a continuous upward trend for the displacement efficiency with varying rates while the displacing fluid encounters different throat sizes and/or gas saturations. Major recovery occurs shortly before breakthrough, when 24.2% of the gas is displaced. A slight increment in gas displacement also occurs after the breakthrough time. The system reaches steady state conditions in 340 s from the start of injection, and no additional gas displacement is observed afterwards.

3.4. Cleat network permeability

Absolute permeability of the microfluidic chip is measured both experimentally and numerically and the results are found to be 20 md and 36 md, respectively. To measure absolute permeability via microfluidic experiments, the entire cleat system needs to be filled with a single phase fluid. However the existence of dead-end pores in the cleat structure makes it difficult to obtain a network fully occupied with water. The discrepancy of absolute permeability values in microfluidic experiment and numerical simulation is assumed to be due to the effect of these unconnected pores on the fluid flow. To obtain more realistic results in our measurements, we use the absolute permeability of 36 md, obtained from the numerical simulations. The numerical simulation of flow in a porous medium consists of calculations of pressure and velocity fields in a discretized form (Mostaghimi et al., 2014; Mostaghimi and Mahani, 2010). A 2-dimensional flow simulation, with a 3.52 μm image resolution of the structure is used; Fig. 9 demonstrates the pressure and velocity profiles obtained from numerical simulations of flow and applying a no-slip boundary on the solid surfaces. The numerical method assumes each pixel as a finite volume grid block and solves the Stokes and continuity equations (Mostaghimi et al., 2012, 2013).

Basically there are two unique parallel fractures where the majority of flow occurs in the fracture with larger throat entry size, and develops to saturate half of the model first with non-wetting phase (see image 5 in Fig. 8). Then, the fluid stream penetrates to the other fracture.

The relative permeability function for the fabricated chip is measured and calculated, as described in Section 2.4 and compares well to other Australian coals (Fig. 10). It is common to plot the relative permeability curve as a function of water saturation (Dake, 1983), and gas saturation is simply related to the water saturation as $S_g = 1 - S_w$. The graph shows that relative permeability increases with increasing water phase saturation. The gas flow rate is calculated based on the difference between inlet and outlet liquid rates; then it is used in Eq. (1) to estimate the gas relative permeability for a given saturation.

Relative permeability of water starts from residual water saturation of 0.60, and increases along with water production after breakthrough.

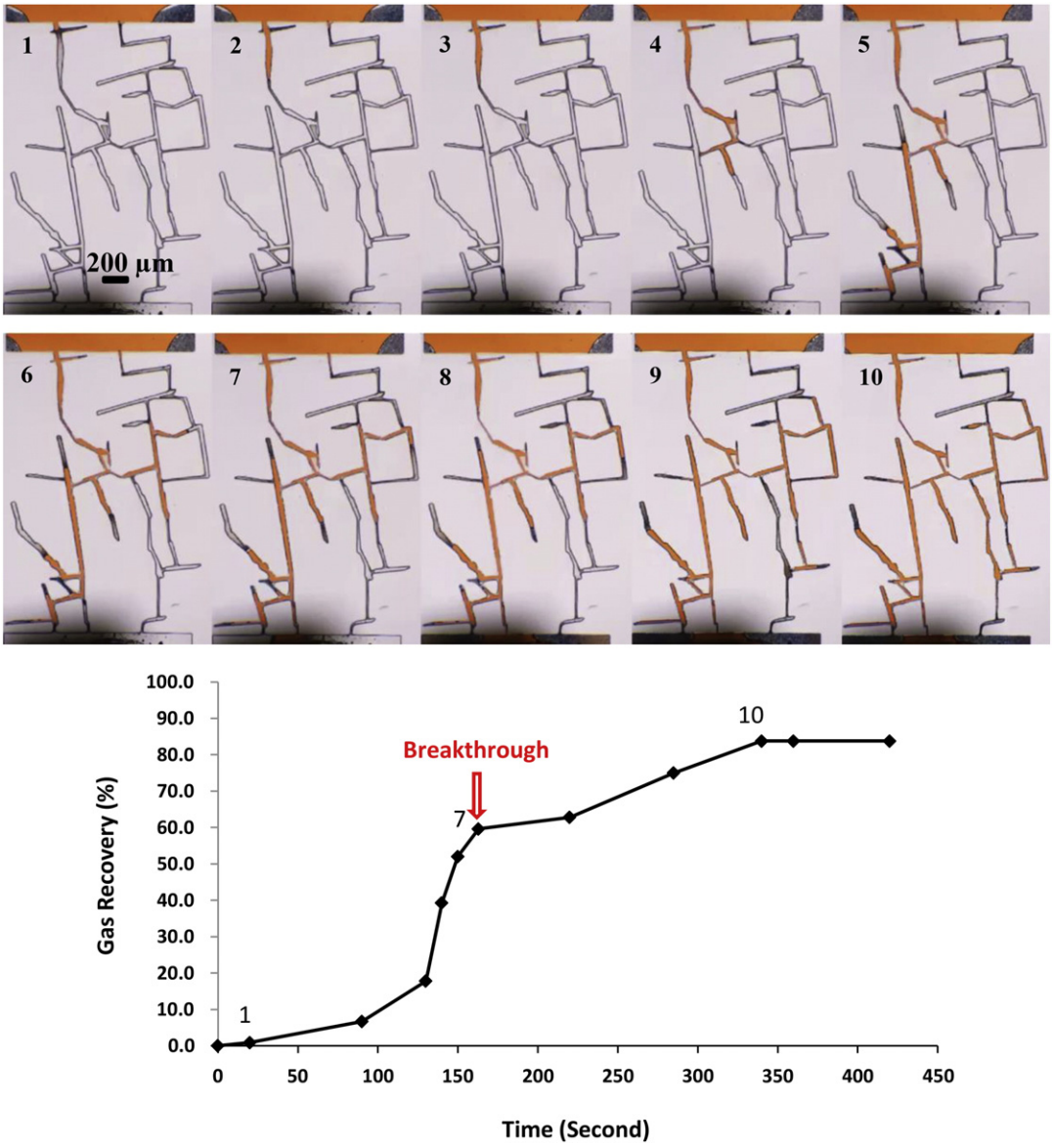

Fig. 8. Injection of the dyed water into a replicated coal porous medium, which is saturated with air (upper images). Sequential images demonstrate the filling behaviour from the start of injection until the system reaches steady state. Gas recovery curve over time in a gas-wet coal is illustrated (lower graph). Numbers on the graph correspond to the filling step.

Water relative permeability end point, which is the maximum value of relative permeability during displacement, is obtained as 0.15, when the system reaches steady state. The residual saturation of gas is obtained as 0.16 which is 3.7 times less than the residual saturation of water in this gas-wet system. After 340 s from the injection, no more displacement occurred. The water and gas relative permeability cross point occurs at $S_w = 0.61$ and $K_w = 0.09$. The cross point indicates where equal flow rates are achieved for both phases. Water production is always a main issue in coal seam methane extraction, which raises both environmental and financial concerns. Meanwhile, the rate of gas recovery from a reservoir needs to meet market demands to make the investment economically reasonable. By understanding and obtaining relative permeability, we can estimate water and gas production rates. This study is the first step in visualizing relative permeability behaviour in a real coal porous structure. The results and data can aid the development of simulations and recovery methods to optimize gas production while minimizing water production.

The relative permeability values obtained from literature (Chen et al., 2014) for Australian coals are also provided in Fig. 10 and demonstrate that the present workflow can provide smooth relative permeability functions that are within the range of other Australian coals. While this is not validation of the measured relative permeability function it however provides confidence that microfluidic chips can be employed as a platform from which the relationship between coal cleat structure and the resulting phase permeability can be studied.

Furthermore, we substantiate our results by calculating the relative permeability of the larger 3D coal core from which the microfluidic chip was modelled after. For the pore network simulation, the contact angle is set to 73° (as observed in the microfluidic experiments). The pore network modelling results correspond well to the measured experimental results and further validate our method and workflow for studying flow in coal cleats. The numerical results indicate higher permeability and lower gas residual saturations, which could be due to higher connectivity of the cleat structure in 3D in comparison with the 2D microfluidic results.

The results of the water relative permeability profile indicate a sharp increase right after breakthrough, which is due to the network

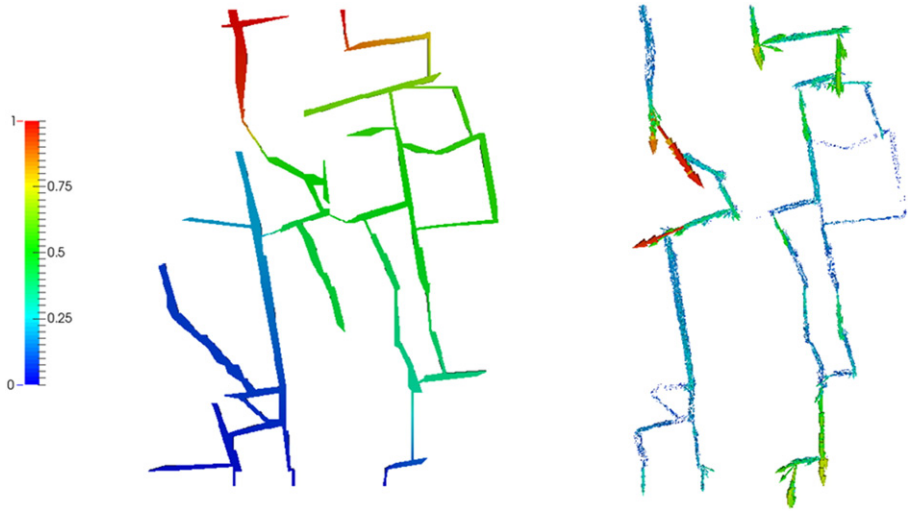

Fig. 9. Pressure profile (left picture) and velocity profile (right picture) of fluid flow in the fabricated coal porous structure, obtained from two-dimensional flow simulation to measure absolute permeability.

geometry with low connectivity and few inlet/outlet throats, which avoids extensive displacement in the pore spaces especially at breakthrough time. In this work we used PDMS with a constant contact angle representing the coal surface wettability. According to literature (Saghafi et al., 2014) however the contact angle is not fixed for coal reservoirs and varies with pore network pressure and coal type. Also, the coal cleat network used in our experiment is fully saturated with gas and the existence of partial water saturation within the coal cleat network is ignored. The cleat network permeability evolution of coal depends on the effect of solid matrix deformation and mechanical stress (Liu et al., 2013). Adsorption and desorption can cause coal matrix swelling and shrinkage respectively, thus affecting permeability values (Brochard et al., 2012; Mazumder and Wolf, 2008). The permeability of coal also associates with differential pressure of external stress, uniaxial strain condition, and pore pressure (Liu et al., 2013). These effects will be the focus of our future studies where a geo-material chip will be used to explore the effect of sorption and high pressure deformations on relative permeability values.

4. Conclusions

We develop a novel microfluidic approach to study transport mechanisms in coal from coal seam gas developments. Advanced imaging techniques were used to resolve the coal cleat system at the micro-scale, and state-of-the-art fabrication methods were used to replicate coal cleat patterns inside microfluidic chips. Relative permeability curves, as the most important parameter for optimizing gas recovery and reducing water production, were measured. Microfluidic experiments provide the advantage of real-time transport observations, and production data measurements for a variety of cleat networks in a fast and cost efficient manner. A water relative permeability end point of 0.15 was measured with residual gas saturation of 0.16. Higher permeability and lower residual saturation measured by pore network modelling are due to more connectivity of pores and cleats in the extracted network as it is conducted on three dimensional micro-CT images where the experimental model refers to cleat pattern in one thin section of the coal sample. The presented relative permeability data

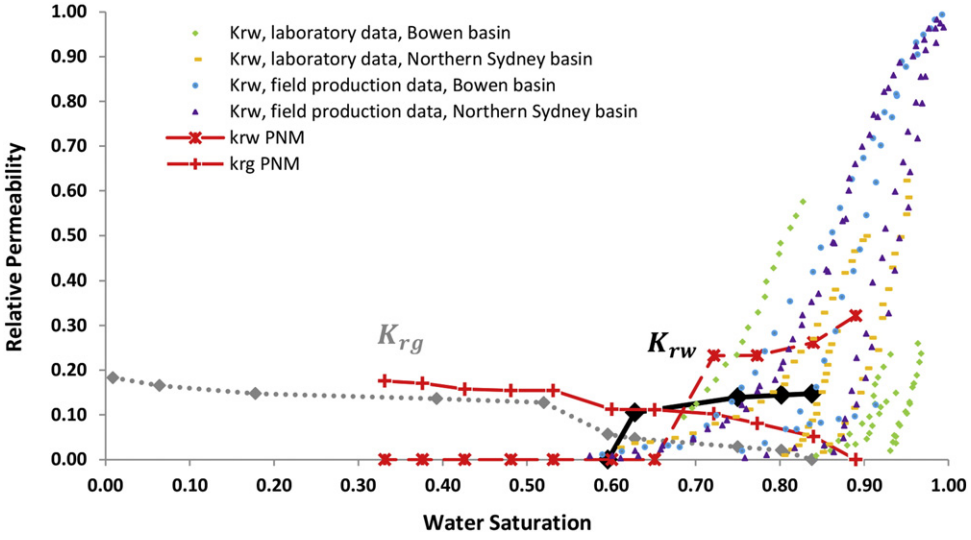

Fig. 10. Comparison of experimental and numerical relative permeability curves of gas-wet medium for the Moura coal sample. Water relative permeability (black) and gas relative permeability (grey) curve versus water saturation, as measured from micro-fluidic experiments, and red lines correspond to results from pore network simulations on a larger 3D subsection of Moura coal.

can be employed for developing direct numerical simulations of multiphase transport in coal beds. In addition, the framework can be applied for understanding the relationship between coal cleat structure and the resulting relative permeability and interpreting larger scale experiments. Due to the small cleats aperture sizes, poor connectivity and low permeability of coals, a wider range of imaged cleat networks can be applied to establish a correlation between cleat topology and relative permeability curve, which will be the focus of our future work.

Acknowledgements

This work was performed (in part) at the South Australian and Queensland node of the Australian National Fabrication Facility under the National Collaborative Research Infrastructure Strategy to provide nano and microfabrication facilities for Australian researchers. Mostaghimi, Armstrong and Warkiani acknowledge financial support from the University of New South Wales, through the Early Career Research (ECR) funding scheme.

References

Ataie-Ashtiani, B., Majid Hassanizadeh, S., Celia, M.A., 2002. Effects of heterogeneities on capillary pressure–saturation–relative permeability relationships. J. Contam. Hydrol. 56, 175–192.

Geoscience Australia, 2009. Coal Seam Gas Fact Sheet, The Australian Atlas of Mineral Resources, Mines, and Processing Centres.

Avraam, D.G., Payatakes, A.C., 1999. Flow mechanisms, relative permeabilities, and coupling effects in steady-state two-phase flow through porous media. The case of strong wettability. Ind. Eng. Chem. Res. 38, 778–786.

Bakke, S., Øren, P.-E., 1997. 3-D pore-scale modelling of sandstones and flow simulations in the pore networks. SPE J. 2, 136–149.

Blunt, M.J., 2000. An empirical model for three-phase relative permeability. SPE J. 5, 435–445.

Blunt, M.J., 2001. Flow in porous media—pore-network models and multiphase flow. Curr. Opin. Colloid Interface Sci. 6 (3), 197–207.

Blunt, M.J., Jackson, M.D., Piri, M., Valvatne, P.H., 2002. Detailed physics, predictive capabilities and macroscopic consequences for pore-network models of multiphase flow. Adv. Water Resour. 25 (8), 1069–1089.

Blunt, M.J., Bijeljic, B., Dong, H., Gharbi, O., Iglauer, S., Mostaghimi, P., Paluszny, A., Pentland, C., 2013. Pore-scale imaging and modelling. Adv. Water Resour. 51, 197–216.

Brochard, L., Vandamme, M., Pellenq, R.J.M., Fen-Chong, T., 2012. Adsorption-induced deformation of microporous materials: coal swelling induced by CO_2–CH_4 competitive adsorption. Langmuir 28, 2659–2670.

Chapman, E.M., Yang, J., Crawshaw, J.P., Boek, E.S., 2013. Pore scale models for imbibition of CO_2 analogue fluids in etched micro-model junctions using micro-fluidic experiments and direct flow calculations. Energy Procedia 37, 3680–3686.

Chen, D., Pan, Z., Liu, J., Connell, L.D., 2013. An improved relative permeability model for coal reservoirs. Int. J. Coal Geol. 109-110, 45–57.

Chen, D., Shi, J.-Q., Durucan, S., Korre, A., 2014. Gas and water relative permeability in different coals: model match and new insights. Int. J. Coal Geol. 122, 37–49.

Dabbous, M.K., Reznik, A.A., Taber, J.J., Fulton, P.F., 1974. The permeability of coal to gas and water. Soc. Pet. Eng. J. 14, 563–572.

Dake, L.P., 1983. Fundamentals of Reservoir Engineering. pp. 117–119.

de Haas, T.W., Fadaei, H., Guerrero, U., Sinton, D., 2013. Steam-on-a-chip for oil recovery: the role of alkaline additives in steam assisted gravity drainage. Lab Chip 13, 3832–3839.

Dicks, A.L., Diniz da Costa, J.C., Simpson, A., McLellan, B., 2004. Fuel cells, hydrogen and energy supply in Australia. J. Power Sources 131, 1–12.

Dong, H., Blunt, M.J., 2009. Pore-network extraction from micro-computerized-tomography images. Phys. Rev. E 80, 036307.

Fadaei, H., Scarff, B., Sinton, D., 2011. Rapid microfluidics-based measurement of CO_2 diffusivity in bitumen. Energy Fuel 25, 4829–4835.

Gash, B.W., 1991. Measurement of "rock properties" in coal for coalbed methane production. SPE Annual Technical Conference and Exhibition, 6–9 October, Dallas, Texas. Society of Petroleum Engineers.

Golab, A., Ward, C.R., Permana, A., Lennox, P., Botha, P., 2013. High-resolution three-dimensional imaging of coal using microfocus X-ray computed tomography, with special reference to modes of mineral occurrence. Int. J. Coal Geol. 113, 97–108.

Gunda, N.S., Bera, B., Karadimitriou, N.K., Mitra, S.K., Hassanizadeh, S.M., 2011. Reservoir-on-a-chip (ROC): a new paradigm in reservoir engineering. Lab Chip 11, 3785–3792.

Hamawand, I., Yusaf, T., Hamawand, S.G., 2013. Coal seam gas and associated water: a review paper. Renew. Sust. Energ. Rev. 22, 550–560.

Harpalani, S., Chen, G., 1995. Estimation of changes in fracture porosity of coal with gas emission. Fuel 74, 1491–1498.

Harpalani, S., Chen, G., 1997. Influence of gas production induced volumetric strain on permeability of coal. Geotech. Geol. Eng. 15, 303–325.

Harpalani, S., Schraufnagel, R.A., 1990. Shrinkage of coal matrix with release of gas and its impact on permeability of coal. Fuel 69, 551–556.

Hawthorne, W., 1975. Regional coal geology of the Bowen Basin. Econ. Geol. Aust. P. N. G. 2, 68–77.

Joseph, J., Siva Kumar Gunda, N., Mitra, S.K., 2013. On-chip porous media: porosity and permeability measurements. Chem. Eng. Sci. 99, 274–283.

Karadimitriou, N.K., Joekar-Niasar, V., Hassanizadeh, S.M., Kleingeld, P.J., Pyrak-Nolte, L.J., 2012. A novel deep reactive ion etched (DRIE) glass micro-model for two-phase flow experiments. Lab Chip 12, 3413–3418.

Karadimitriou, N.K., Musterd, M., Kleingeld, P.J., Kreutzer, M.T., Hassanizadeh, S.M., Joekar-Niasar, V., 2013. On the fabrication of PDMS micromodels by rapid prototyping, and their use in two-phase flow studies. Water Resour. Res. 49, 2056–2067.

Kirby, B.J., 2010. Micro- and Nanoscale Fluid Mechanics: Transport in Microfluidic Devices. pp. 60–66.

Korsch, R.J., Boreham, C.J., Totterdell, J.M., Shaw, R.D., 1998. Development and petroleum resource evaluation of the Bowen, Gunnedah and Surat basins, eastern Australia. APPEA J. 38, 199–237.

Lamei Ramandi, H., Mostaghimi, P., Armstrong, R.T., Saadatfar, M., Pinczewski, W.V., 2016. Porosity and permeability characterization of coal – a micro-computed tomography study. Int. J. Coal Geol. 154–155, 57–68.

Latham, S., Varslot, T., Sheppard, A., 2008. Image registration: enhancing and calibrating X-ray micro-CT imaging. International Symposium of the Society of Core Analysts, Abu Dhabi, UAE.

Laubach, S.E., Marrett, R.A., Olson, J.E., Scott, A.R., 1998. Characteristics and origins of coal cleat: a review. Int. J. Coal Geol. 35, 175–207.

Lele, P., Fadaei, H., Guerrero, U., Sinton, D., 2014. Development of a microfluidic device for rapid assessment of EOR additives. SPE Heavy Oil Conference-Canada, 10–12 June, Calgary, Alberta, Canada. Society of Petroleum Engineers.

Lenormand, R., Zarcone, C., Sarr, A., 1983. Mechanisms of the displacement of one fluid by another in a network of capillary ducts. J. Fluid Mech. 135, 337–353.

Liu, S., Harpalani, S., Wang, Y., 2013. Deformation characteristics of coal and its impact on permeability during CO_2 sequestration. International Conference on Coal Science & Technology, USA.

Mahoney, S.A., Rufford, T.E., Dmyterko, A.S.K., Rudolph, V., Steel, K.M., 2015a. The effect of rank and lithotype on coal wettability and its application to coal relative permeability models. SPE Asia Pacific Unconventional Resources Conference and Exhibition, Brisbane, Australia.

Mahoney, S.A., Rufford, T.E., Rudolph, V., Liu, K.-Y., Rodrigues, S., Steel, K.M., 2015b. Creation of microchannels in Bowen Basin coals using UV laser and reactive ion etching. Int. J. Coal Geol. 144–145, 48–57.

Mallett, C.W., Pattison, C., McLennan, T., 1995. Geology of Australian coal basins. Special Publication-Geological Society of Australia, Coal Geol. Group, 1.

Mason, G., Morrow, N.R., 1991. Capillary behavior of a perfectly wetting liquid in irregular triangular tubes. J. Colloid Interface Sci. 141, 262–274.

Mazumder, S., Wolf, K.H., 2008. Differential swelling and permeability change of coal in response to CO_2 injection for ECBM. Int. J. Coal Geol. 74, 123–138.

Meaney, K., Paterson, L., 1996. Relative permeability in coal. SPE Asia Pacific Oil and Gas Conference, 28–31 October, Adelaide, Australia. Society of Petroleum Engineers.

Mostaghimi, P., Mahani, H., 2010. A quantitative and qualitative comparison of coarse-grid-generation techniques for modeling fluid displacement in heterogeneous porous media. SPE Reserv. Eval. Eng. 13 (01), 24–36.

Mostaghimi, P., Bijeljic, B., Blunt, M., 2012. Simulation of flow and dispersion on pore-space images. SPE J. 17, 1,131–131,141.

Mostaghimi, P., Blunt, M., Bijeljic, B., 2013. Computations of absolute permeability on micro-CT images. Math. Geosci. 45, 103–125.

Mostaghimi, P., Tollit, B.S., Neethling, S.J., Gorman, G.J., Pain, C.C., 2014. A control volume finite element method for adaptive mesh simulation of flow in heap leaching. J. Eng. Math. 87 (1), 111–121.

Mostaghimi, P., Armstrong, R.T., Gerami, A., Warkaini, M.E., Ramandi, H.L., Pinczewski, V., 2015. Micro-CT imaging and microfluidics for undrestanding flow in coal seam reservoirs. International Symposium of the Society of Core Analysts, Newfoundland, Canada.

Nguyen, P., Fadaei, H., Sinton, D., 2013. Microfluidics underground: a micro-core method for pore scale analysis of supercritical CO_2 reactive transport in Saline aquifers. J. Fluids Eng. 135, 021203.

Oren, P.-E., Bakke, S., Arntzen, O.J., 1998. Extending predictive capabilities to network models. SPE J. 3, 324–336.

Pan, Z., Connell, L.D., 2012. Modelling permeability for coal reservoirs: a review of analytical models and testing data. Int. J. Coal Geol. 92, 1–44.

Pan, Z., Connell, L.D., Camilleri, M., 2010. Laboratory characterisation of coal reservoir permeability for primary and enhanced coalbed methane recovery. Int. J. Coal Geol. 82, 252–261.

Pant, L.M., Mitra, S.K., Secanell, M., 2012. Absolute permeability and Knudsen diffusivity measurements in PEMFC gas diffusion layers and micro porous layers. J. Power Sources 206, 153–160.

Porter, M.L., Jimenez-Martinez, J., Martinez, R., McCulloch, Q., Carey, J.W., Viswanathan, H.S., 2015. Geo-material microfluidics at reservoir conditions for subsurface energy resource applications. Lab Chip 15, 4044–4053.

Purl, R., Evanoff, J.C., Brugler, M.L., 1991. Measurement of coal cleat porosity and relative permeability characteristics. SPE Gas Technology Symposium, 22–24 January, Houston, Texas. Society of Petroleum Engineers.

Radlinski, A.P., Mastalerz, M., Hinde, A.L., Hainbuchner, M., Rauch, H., Baron, M., Lin, J.S., Fan, L., Thiyagarajan, P., 2004. Application of SAXS and SANS in evaluation of porosity, pore size distribution and surface area of coal. Int. J. Coal Geol. 59, 245–271.

Robertson, E.P., Christiansen, R.L., 2006. A Permeability Model for Coal and Other Fractured, Sorptive-Elastic Media. SPE-104380-MS 13. pp. 314–324.

Saghafi, A., Javanmard, H., Pinetown, K., 2014. Study of coal gas wettability for CO_2 storage and CH_4 recovery. Geofluids 14, 310–325.

Schmidt, K.A.G., Folas, G.K., Kvamme, B., 2007. Calculation of the interfacial tension of the methane–water system with the linear gradient theory. Fluid Phase Equilib. 261, 230–237.
Silin, D., Patzek, T., 2006. Pore space morphology analysis using maximal inscribed spheres. Physica A: Stat. Mech. Appl. 371, 336–360.
Song, W., de Haas, T.W., Fadaei, H., Sinton, D., 2014. Chip-off-the-old-rock: the study of reservoir-relevant geological processes with real-rock micromodels. Lab Chip 14, 4382–4390.
Squarek, J., Dawson, M., 2006. Coalbed methane expands in Canada. Oil Gas J. 37–40.
Vargaftik, N.B., Volkov, B.N., Voljak, L.D., 1983. International tables of the surface tension of water. J. Phys. Chem. 12.
Wang, G.X., Massarotto, P., Rudolph, V., 2009. An improved permeability model of coal for coalbed methane recovery and CO_2 geosequestration. Int. J. Coal Geol. 77, 127–136.
Warkiani, M.E., Lou, C.-P., Gong, H.-Q., 2011. Fabrication of multi-layer polymeric micro-sieve having narrow slot pores with conventional ultraviolet-lithography and micro-fabrication techniques. Biomicrofluidics 5, 036504.
Williams, J., Stubbs, T., Milligan, A., 2012. An analysis of coal seam gas production and natural resource management in Australia. A Report Prepared for the Australian Council of Environmental Deans and Directors by John Williams Scientific Services Pty Ltd, Canberra, Australia.
Xu, W., Ok, J.T., Xiao, F., Neeves, K.B., Yin, X., 2014. Effect of pore geometry and interfacial tension on water-oil displacement efficiency in oil-wet microfluidic porous media analogs. Phys. Fluids 26, 093102.
Zhang, J., Feng, Q., Zhang, X., Wen, S., Zhai, Y., 2014. Relative permeability of coal: a review. Transp. Porous Media 106, 563–594.
Zhang, Y., Gong, B., Li, J., Li, H., 2015. Discrete fracture modeling of 3D heterogeneous enhanced coalbed methane recovery with prismatic meshing. Energies 8, 6153.
Zou, M., Wei, C., Yu, H., Song, L., 2015. Modeling and application of coalbed methane recovery performance based on a triple porosity/dual permeability model. J. Nat. Gas Sci. Eng. 22, 679–688.